Lung metastases detection in CT images using 3D template matching

Peng Wang
Department of Biomedical Engineering, University of Rochester, Rochester, New York 14642

Andrea DeNunzio
Department of Bioengineering, University of Pennsylvania, Philadelphia, Pennsylvania 19104

Paul Okunieff
Department of Radiation Oncology, University of Rochester, Rochester, New York, 14642

Walter G. O'Dell[a)]
Departments of Biomedical Engineering and Radiation Oncology, University of Rochester, New York, 14642

(Received 27 March 2006; revised 20 November 2006; accepted for publication 22 December 2006; published 9 February 2007)

The aim of this study is to demonstrate a novel, fully automatic computer detection method applicable to metastatic tumors to the lung with a diameter of 4–20 mm in high-risk patients using typical computed tomography (CT) scans of the chest. Three-dimensional (3D) spherical tumor appearance models (templates) of various sizes were created to match representative CT imaging parameters and to incorporate partial volume effects. Taking into account the variability in the location of CT sampling planes cut through the spherical models, three offsetting template models were created for each appearance model size. Lung volumes were automatically extracted from computed tomography images and the correlation coefficients between the subregions around each voxel in the lung volume and the set of appearance models were calculated using a fast frequency domain algorithm. To determine optimal parameters for the templates, simulated tumors of varying sizes and eccentricities were generated and superposed onto a representative human chest image dataset. The method was applied to real image sets from 12 patients with known metastatic disease to the lung. A total of 752 slices and 47 identifiable tumors were studied. Spherical templates of three sizes (6, 8, and 10 mm in diameter) were used on the patient image sets; all 47 true tumors were detected with the inclusion of only 21 false positives. This study demonstrates that an automatic and straightforward 3D template-matching method, without any complex training or postprocessing, can be used to detect small lung metastases quickly and reliably in the clinical setting. [DOI: 10.1118/1.2436970]

Key words: lung tumor, computed tomography, computer-aided diagnosis, lung metastases

INTRODUCTION

The lung is the most frequent site of primary cancer and lung cancer is the leading cause of cancer death in the U.S.[1] In addition, the lung is a frequent site of metastatic disease and the majority of cancer patients today die of metastatic disease rather than the uncontrolled growth of the primary cancer. For example, among women who die of breast cancer, 57–77% have metastases to the lung,[2] and the lungs are exceeded only by bone as the most common sites of metastases.[3] Among those patients who die of colorectal cancers, almost half have lung metastases,[4] and among those succumbing of sarcoma or of head and neck cancer, almost all have lung metastases.

In the early stage of lung metastases, the number and locations of metastatic tumors are usually limited, a concept termed oligometastases. It is also hypothesized that late-onset metastatic tumors may be derived from the early-onset lesions, and therefore eliminating the first stage of metastatic disease could greatly ameliorate the development of secondary metastatic tumors. Unfortunately, traditionally the utility of radiation to control lung disease has been limited by the lungs' poor radio-tolerance. Recent advances in hypofractionated, conformal, high-dose stereotactic radiosurgery/radiation therapy have made it possible to deliver lethal radiation doses to surgically precise locations, thereby expanding the size of lesions that are treatable and the scope of patients who can be considered as candidates for curative treatment of their cancer.[5] This technique has been applied in our institute using a Novalis Shaped Beam Surgery System (BrainLAB AG, Heimstetten, Germany) to treat extra-cranial metastatic tumors since 2001 and achieved local control rates of 88% for metastases to the liver[6] and 94% for metastases to the lung.[7]

The application of stereotactic radiosurgery to pulmonary targets (PSRTs) opens the door for curative treatment of lung cancer and for improving the survival of patients with metastases, but only if the tumors can be detected at a stage where they are small enough to enable the use of lethal radiation dose levels. At small sizes, however, the presence of metastatic tumors is not discerned by the patient and not detectable using clinical pulmonary function tests, hence the need for lung tumor screening via medical imaging. Three-dimensional (3D) medical imaging modalities, specifically serial section x-ray CT and magnetic resonance imaging

TABLE I. Detection rate and false positive rate for recently published results from the literature (*NA*=data not available). All results shown are for human data.

Group	No. of datasets	No. of slices	Slice thickness (mm)	No. of nodules	Nodule diameters (mm)	% nodules detected	No. of false positives per nodule	No. of false positives per slice
Lee 2001	20	557	10	98	5–30	72%	6.28	1.10
Zhao 2003	1	~30	7	4	~10	75%	2.25	0.30
Arimura 2004	106	3292	10	131	6–26	81%	5.91	0.28
McCulloch 2004	50	NA	2.5	43	5.0–17.1	70%	9.65	NA
Lee 2004	15	4122	1.25–2	309	2–30	81%	1.40	0.10
Lin 2005	29	583	10	393	10–30	89.3%	0.31	0.21
Armato 2005	393	11 029	10	470	*NA*	70%	37.5	1.6
Ge 2005	82	3551	1.0–2.5	116	3.0–30.6	95.7%	11.3[a]	0.37[a]

[a]At 80% sensitivity.

(MRI), have become increasingly popular for screening of pulmonary cancer. Large clinical trials are underway to detect early lesions by CT screening of high risk populations.[8,9]

Serial section CT has been shown to increase lung tumor detection rates by 300–500%, compared with radiologists' results using only projection chest x rays,[8,10,11] and the average size of tumors detected has been reduced from 30 to 12 mm.[12] Whereas a thoracic CT scan using a single detector scanner typically generates 40 to 100 axial image slices, the newer, multi-detector scanners typically generate 300 to 600 image slices. To read and interpret these massive amounts of image data requires a substantial amount of radiologist effort and predisposes the screening process to human error and missed detection of cancerous lesions. Swensen *et al.*[13] found that when retrospective interpretation of baseline lung images was performed, nodules were found to have been initially missed in 26% of subjects. A chief concern is the nodules of small size, low contrast, or those located near vessel structures, since these nodules are often missed by the unaided radiologist.[14–16] Thus, computer-aided diagnostic (CAD) approaches are becoming increasingly necessary for both reducing radiologists' effort and improving detection sensitivity.

Various CAD methods have been proposed to detect lung nodules from serial section image sets. A summary of recent lung CAD results is presented in Table I.[17–24] Most methods consist of three steps: (1) *preprocessing*: segmentation of lung field, filtering of data, etc.; (2) *selection* of initial nodule candidates; and (3) *postprocessing*: analyzing features of initial nodule candidates and eliminating false positives. The existing CAD methods can be divided into two major groups based on the different strategies used in nodule selection and analysis: intensity based and feature based (model based). Intensity-based methods distinguish initial lung nodule candidates from lung parenchyma by their relative high intensity in CT images. This step can be done in 2D (slice-by-slice processing) or in 3D (3D segmentation). Then additional features of each initial candidate are extracted, including 2D features such as area, eccentricity, circularity, irregularity, and compactness, and 3D features such as volume, sphericity, 3D compactness, and mean intensity value. Classifiers are then applied on those features to exclude false positives. Examples of intensity-based methods are region growing,[21,25,26] combination of attenuation thresholding and region growing,[27,28] fuzzy clustering,[22,29] K-mean clustering,[24] and gray-scale thresholding.[18,19,23,27,30–34] Feature-based methods take into consideration the nodules' compact spherical shape, together with other information such as overall size, density, texture, etc., to establish models of lung nodules. Examples are model-based similarity measures,[35] pattern classification,[36] template matching using a genetic algorithm,[17,37] "N-Quoit" spatial filtering,[38] object-based deformation,[39] morphological analysis,[40] multistage anatomic model,[20] and patient-specific models.[41] Results from these and related CAD algorithms are encouraging in general; however, most current CAD schemas suffer from a miss-rate of 10–30% (low sensitivity) and, at the same time, generate a large number of false positives (low specificity). A high false positive rate is undesirable because it defeats the objective of reducing the effort required of the attending radiologist. Moreover, it is quite unfavorable for a CAD method to miss detecting a tumor that is present in a patient.

The primary challenge for radiologists and CAD systems alike for lung tumor detection is that in cross-sectional images there are many objects that have the same appearance and voxel intensity as tumor nodules. Most of these objects are blood vessels coursing obliquely through the image plane. In a cross-sectional slice, a cylindrical vessel can appear circular, and many vessels in the lung have a similar diameter to the tumors of interest. Except for Lee *et al.*[17] (for which a detailed comparison is provided in the Discussion section), a primary failing point of most CAD systems referenced above is that they depend upon a first-pass detection of candidates based on 2D image features, producing hundreds of first-pass candidates. The CAD systems then employ various schemes to tackle the enormous task of removing likely false positives from the vast candidate pool, with varying degrees of success. A common problem is that in filtering out the large volume of false positives, true positives are also omitted, creating a system that is prone to missing true tumors yet maintains a relatively high false positive count.

The approach described herein was motivated by the observation that experienced radiologists screen for lung tumors not by considering individual image slices indepen-

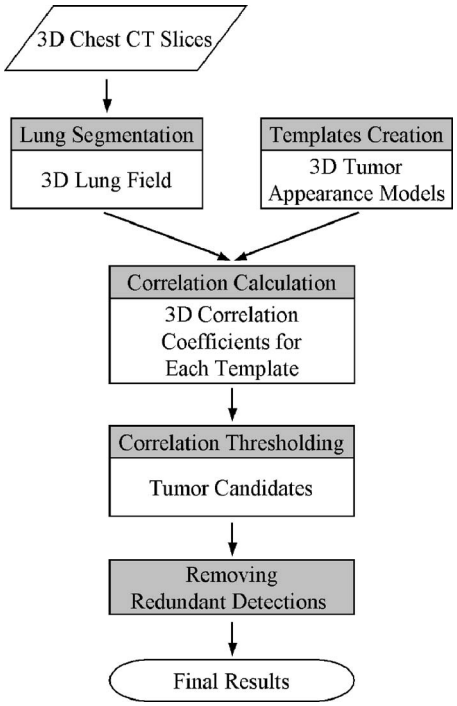

FIG. 1. Flowchart of the 3D template-based detection algorithm. Shown in gray blocks are the processes, followed by the resultant outcome at each step.

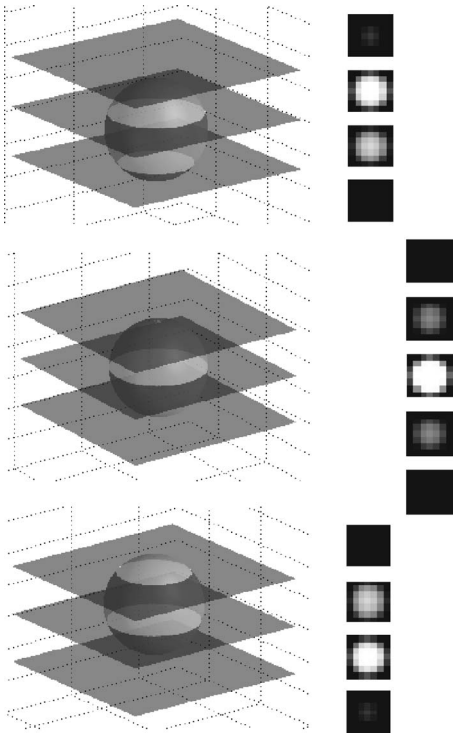

FIG. 2. Models of the appearance of a uniform-density 6 mm diameter sphere on consecutive 3 mm thick image slices. Left side: depiction of 3D sphere model and image cut-planes. Right side: appearance of sphere in consecutive simulated image slices, with 1×1 mm in-plane pixel dimensions and including partial volume effects. Middle pair: Instance where the central cut-plane intersects the sphere exactly through the center. Top pair: the cut-planes are offset by +1 mm ($\frac{1}{3}$ of the slice thickness) vertically. Bottom pair: the cut-planes are offset by −1 mm vertically.

dently, but by paging through the image stack looking for 3D appearance characteristics that distinguish tumors from vessels. On consecutive images, vessels maintain a similar cross-sectional size and their in-plane circular appearance appears to drift across the viewing screen from one slice to the next, following the tortuous anatomy of the vessel. True lung tumors, in contrast, appear as circular objects that remain at approximately the same on-screen location from slice to slice. Their size quickly increases and then just as rapidly decreases and the tumor disappears after a few slices. In essence the radiologist is constructing in his/her mind a 3D model of the tumor anatomy and the interaction of that 3D object with the serial image slices. The new approach is to construct a 3D model of the imaging features of a spherical tumor and then to perform a search through the 3D imaging volume for objects that are similar to our 3D tumor appearance model. In this study, our aim is automatic detection of tumors 4–13 mm in diameter in the lungs of patients at high-risk for developing metastatic disease. The purpose of this work is to determine the optimal parameters for tumor appearance models and the detection capture range in regards to tumor size, tumor eccentricity, and image quality using simulated image datasets, and to establish the sensitivity and specificity of our algorithm in human lung datasets.

METHODS

Overall scheme of the detection algorithm

A flowchart of our fully automatic CAD method is shown in Fig. 1.

3D tumor appearance model (template)

To demonstrate a typical 3D case, Fig. 2 shows an appearance model sphere for a tumor 6 mm in diameter of uniform density that was constructed on a dark background. The imaging parameters were chosen based on a representative patient image dataset: in-plane pixel size of 1×1 mm and slice thickness and slice separation of 3 mm. Figure 2 shows the results for the instance when a CT image slice intersects the exact center of the sphere (middle of figure) and with the image slices offset by plus (top of figure) and minus (bottom of figure) $\frac{1}{3}$ of the slice thickness. The partial volume of the sphere in each voxel was taken into consideration for each slice that is intersected by the sphere to give variable gray-scale voxel intensities both in-plane and through the slice thickness. An optimal in-plane padding (determined in simulation) was added to each tumor appearance model. An out-of-plane padding slice was added whenever an end slice average intensity value was more than a maximum threshold of 20%. Thus the centrally located tumor model was given an out-of-plane padding slice at both ends, while the two offset models typically included a padding slice at one end, as depicted in Fig. 2.

Lung segmentation

To speed up the computation, an automatic lung segmentation procedure was performed to remove from consider-

ation objects outside the lung region. An initial histogram-based thresholding step isolated the lung parenchyma from the surrounding soft tissue and bones. This was followed by a series of morphological operations that remove from within the lung space the vessels, lesions, and other relatively small objects. The resulting modified binary image was then used as a mask to extract out only the lung tissue, over which the search for tumor candidates was then performed. In order to include into the analysis tumors attached to pleura, 3D morphological operations (including opening/closing) were applied on the initial lung mask.

3D correlation calculation

The next task was to search the serial lung image stack for 3D objects that match the 3D appearance model. This was essentially a 3D template-matching scheme to evaluate the similarity between subregions around each voxel in the image stack and the templates. A search over the entire lung volume was performed computationally using the 3D normalized cross-correlation coefficient (NCCC) given in Eq. (1). First, the covariance Cov_{xy} was computed by calculating the average and variance for each of two sampled datasets, X and Y. Then the covariance was normalized by dividing by a term involving the individual variances S_{xx}^2 and S_{yy}^2, giving the 3D NCCC.

$$\bar{x} = \frac{1}{n}\sum x_i, \quad \bar{y} = \frac{1}{n}\sum y_i,$$

$$S_{xx}^2 = \frac{1}{n-1}\sum (x_i - \bar{x})^2, \quad S_{yy}^2 = \frac{1}{n-1}\sum (y_i - \bar{y})^2,$$

$$\mathrm{Cov}_{xy} = \frac{1}{n-1}\sum (x_i - \bar{x})(y_i - \bar{y}),$$

$$\mathrm{NCCC} = \frac{\mathrm{Cov}_{xy}}{\sqrt{S_{xx}^2 \cdot S_{yy}^2}}. \tag{1}$$

Here, dataset "X" is the serial slice voxels in the appearance model, and the dataset "Y" is the correspondent subregion voxels in the patient medical image slices. An NCCC value was computed at each lung voxel, as shown in Figs. 3(b) and 3(c). A perfect match is represented by a 1.0 normalized correlation value; a random sampling would give a 0.0 correlation value. Thus local maxima in the correlation results correspond to tumor candidates. To speed up the computation, the calculation of NCCC was accomplished in the Fourier domain of the image and of the template, a method based on the 2D approach by Lewis[42] as used in the MATLAB[43] Image Processing Toolbox. The code was modified by the authors to incorporate a 3D analysis and to improve the memory storage efficiency necessitated by the large amount of image data.

Removing redundant detections

Our approach was to utilize multiple tumor appearance models to capture tumors over a range of sizes. In this approach, it is possible for individual tumors to become matched to multiple tumor appearance models. To eliminate redundant counts we recorded the central location of each tumor, as determined from the local maximum correlation value at each site satisfying the threshold criterion. Two or more detections were considered to come from the same tumor if the central locations were within the radius of the model.

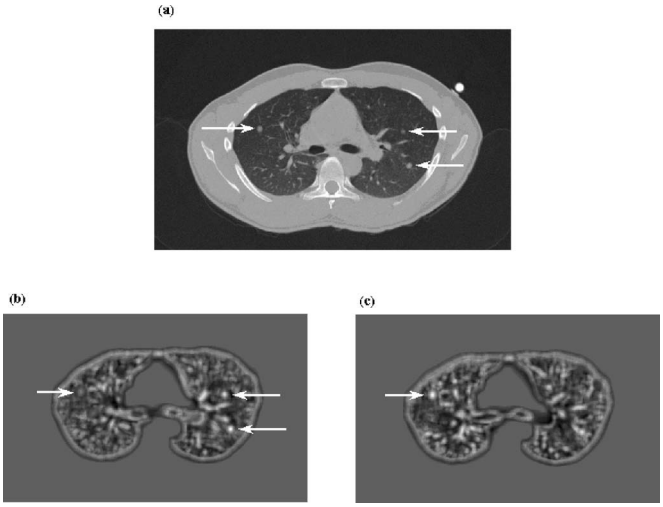

FIG. 3. (a) One slice through the simulated tumor image stack. The three arrows point to simulated tumors. (b) The corresponding correlation map computed using a 6 mm template, at the image slice location in (a). (c) The correlation map at an adjacent slice. The gray-level values at each voxel in the correlation map represent the normalized 3D cross-correlation coefficient between the 3D tumor model of interest and the 3D patient image dataset. The simulated tumor in the upper left of the image (a) is not centered on the current image slice, thus even though the tumor is apparent in the CT image, its correlation match is more apparent on the adjacent slice (c).

Simulated test datasets

For our initial testing phase, realistic human lung image datasets with simulated tumors were generated. To achieve realistic tumor images, simulated spherical tumors with non-integer sizes and ellipsoidal tumors with different eccentricity, orientations, and subslice thickness locations were created. Spherical test tumors were created with diameters in the range 4.1 to 12.5 mm. Ellipsoids (prolate spheroids) were generated with axis ratio ranging from 1.25 to 2.0 and minor axis diameters ranging from 4.5 to 10.5 mm. The resulting computer-generated test tumors were then blurred with a Gaussian filter to mimic the point spread function of the typical clinical imaging scanner. These simulated tumors were then superposed onto the 3D medical image sets of a representative patient and centered at subvoxel positions determined by a random number generator. Finally, the voxel intensity values across the entire image set were given a Gaussian perturbation of varying standard deviation up to twice the intrinsic noise of a typical scan. In this manner datasets were generated with multiple simulated tumors to

determine optimal parameters of templates (size, padding, and threshold) to study the effects of tumor size and image noise on detection performance.

Human datasets

A small-scale study was performed using image data acquired on patients with lung metastases treated using PSRT at the authors' institution. The images were acquired using a standard GE Genesis Lightspeed CT clinical scanner (GE medical system, Milwaukee, Wisconsin) with slice thickness 3 mm, slice separation 3 mm, in-plane resolution 0.9375 mm, tube voltage 120 kV, and tube current 70–120 mA. All images were acquired during a 20–30 s end-expiration breath-hold, with no injected contrast. This imaging protocol is typical of routine follow-up and screening of high-risk patients at the authors' institution. The presence and location of 47 tumors of diameter approximately 4–20 mm across 12 datasets were determined by a radiologist and confirmed by an experienced radiation oncologist. The optimal template parameters determined from the analysis of the simulated tumor datasets were applied on the in-house human datasets.

RESULTS

Tumor size capture range and selection of model parameters

In order to choose the adequate template sizes for the desired tumor detection range, tumor capture range was evaluated using the simulated tumor image sets (Fig. 4). At a typical NCCC cutoff of 0.70, the capture curves for the three templates with diameters 6, 8, and 10 mm overlap with each other to form a continuous spectra covering tumor diameter of 4–13 mm. Using these three sizes, the optimal padding and correlation coefficient thresholds for each size were determined by reducing the number of false positive findings in the simulation image sets while retaining all the simulated tumors. The resultant optimal in-plane paddings were 1, 2, and 2 pixels and correlation thresholds values were 0.75, 0.68, and 0.68 for the 6, 8, and 10 mm models, respectively.

Tumor detection versus image noise on simulated datasets

The addition of Gaussian noise with standard deviation 0, 10, 26, and 52 Hounsfield Units (up to twice that of intrinsic noise) did not alter the detection rate of simulated tumors. Using the optimal paddings and thresholds, the number of false positives (1–2 per case) did not change with the increased noise level.

Tumor detection results on in-house human datasets

The optimal tumor model parameters determined from the simulated tumor datasets were applied to the analysis of human serial CT datasets acquired on patient subjects treated for lung metastases. Twelve patient datasets with 752 image slices and a total of 47 lung tumors ranging from approximately 4 to 20 mm in diameter were processed. Several

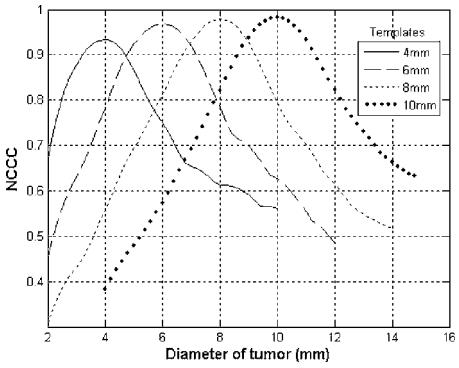

FIG. 4. Tumor size capture range for various-sized appearance models, based on simulated tumor datasets. The horizontal axis is the diameter of the simulated spherical tumor. Plotted on the vertical axis is the *lowest individual NCCC* for any tumor at each diameter. For a given simulated tumor the individual NCCC value is determined by computing the maximum NCCC among the three template varieties. The individual NCCC value varies among the multiple tumors at any given tumor diameter depending on several factors, including the tumor position offset. The highest individual NCCC is found for tumors offset exactly by 0 and $\pm\frac{1}{3}$ slice spacing (identically matching the appearance models, Fig. 2). The lowest individual NCCC occurs for those tumors with the greatest misalignment (offset by $\pm\frac{1}{2}$ slice spacing). The left-most curve represents the lowest individual NCCC for a 4 mm diameter tumor appearance model against simulated tumors of size 2 to 10 mm in diameter. The remaining curves, going from left to right, are the plots for tumor appearance models of 6, 8, and 10 mm diameter, respectively. For example, using a correlation threshold of 0.7 would enable the 6 mm model to detect tumors of size range 3.5 to 9.0 mm diameter, but miss other-sized tumors.

juxta-pleural nodules were present in these datasets and all were correctly excluded from the chest wall during the lung segmentation step. Three templates sizes were used: 6, 8, and 10 mm. For each size, three appearance models were created: one with the tumor model situated exactly in the center of an image plane, one with the model shifted 1 mm above the central cut-plane, and one with the model shifted down 1 mm, as depicted in Fig. 2. Thus, nine appearance models were used to scan the CT image datasets for tumor candidates. The computation of the 3D NCCC for all nine appearance models, each with an approximately 70-slice lung image set, took approximately 5 min on a 1.8 GHz PC running MATLAB version 6.5 with the fast NCCC algorithm. Using the optimal paddings and correlation threshold values determined in the simulation, the algorithm detected all 47 tumors together with the citing of 21 false positives. The false positive rate expressed as the ratio of false positives to true positives was 0.45. The average false positive per patient scan was only 1.8 per case, while the number per image slice, a more common index seen in the literature, was 0.028. Figure 5 shows an example of a patient slice with two real tumors and the corresponding correlation map computed using a 6 mm template.

A FROC analysis was performed producing a curve with a sharp upward slope that achieved a sensitivity of 1.0 (100%) at a false positive rate of 1.8 false positives per CT scan and achieved zero false positives at a sensitivity of 0.26. The low number of false positives resulted in a curve that was not smoothly varying but was inflected where the rate at

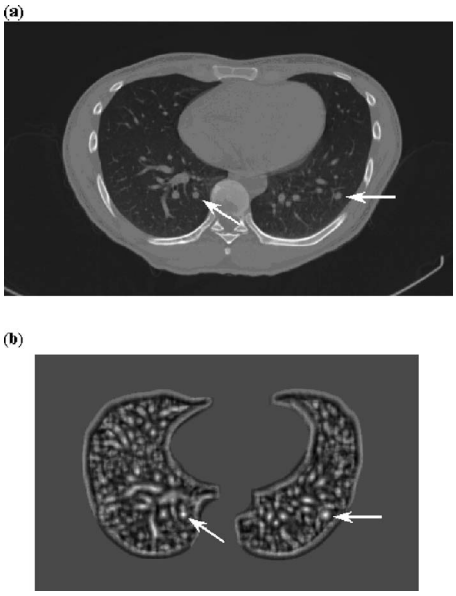

FIG. 5. (a) One slice from a patient scan showing two lung tumors identified by a radiologist, indicated by the white arrows. (b) The corresponding correlation map computed using a 6 mm template, at the image slice location. Though not readily appreciated in this rendering, the centers of the two tumors are the brightest objects in the correlation map.

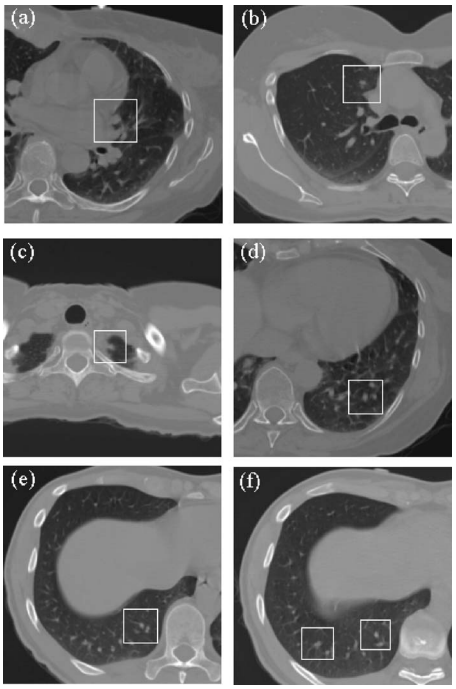

FIG. 6. Examples of false positive findings. The size of each example is 200×200 pixels (187.5×187.5 mm). Shown in the center of each white box is the false positive object. In (a)–(c), false positives occurred at anatomic structures adjacent to pleura and/or cardiac surfaces; in (d), the false positive was a branching region of a blood vessel; and in (e) and (f), false positives occurred in proximity to the diaphragm where respiratory motion artifacts can disrupt the appearance of blood vessels.

which false positives were excluded was not less than the rate at which the true nodules were omitted. This shape and the rapid achievement of 100% sensitivity make FROC analysis a less useful tool for evaluating this approach.

False positive findings

The major sources of false positive findings include structures that are attached to the heart or chest wall, branching/joint regions of thick blood vessels, and blood vessels disrupted by motion artifacts. Figure 6 demonstrates some typical false positives.

DISCUSSION

In summary, a novel 3D template-matching algorithm has been introduced for the automatic detection of small lung tumors from serial CT image slices. The method was based on the construction of 3D models of the appearance of small metastatic tumors in volumetric medical imaging datasets and this method was applicable to standard CT imaging protocols without the need for injected contrast. On patient CT images with tumors ranging from 4 to 20 mm in diameter, the method achieved a 100% detection rate with 1.8 false positives per case. Our algorithm was also shown robust to simulated image noise and was insensitive to variations in the target contrast. Since the normalized cross-correlation coefficient relies on the relative intensity contrast between the tumor and the background tissue, rather than on the physical properties of any individual imaging modality, the detection method can be used with other volumetric imaging modalities such as MRI and 3D ultrasound. It can also be adapted to detect tumors with compact geometry at other anatomic sites, such as brain.[44] Our underlying hypothesis was that small metastatic tumors take on an approximately spherical shape, and this was found to be true much of the time. However, the detection method was found also to be perceptive to highly eccentric simulated tumors and to true tumors that do not appear spherical in shape and that were far larger (up to 20 mm) than the largest appearance model (10 mm). In contrast to previous automatic tumor detection algorithms, the authors' method does not require an elaborate set of classifiers, lengthy training/learning, or complex image preprocessing. This is primarily because our algorithm works intrinsically in three dimensions to select the 3D tumors from 3D image datasets, obviating the collection of numerous first-pass false positives.

The stated aim of this study was to optimize model parameters for the detection of nodules 4–13 mm in diameter. A concern of the template matching approach is that to capture tumors of greater size, a large number of additional templates would be needed, increasing the computational demand. However, as mentioned above, our selected tumor appearance models were able to pick up much larger tumors, with diameters up to 20 mm. In addition, with the increase of tumor size the effect of partial volume is diminished, eliminating the need for the $\pm\frac{1}{3}$ slice offset template varieties. Also, since there are very few normal structures in the lung at larger sizes, the NCCC threshold can be lowered without the risk of increasing the number of false positives. Additional simulations were performed and showed that a central 14 mm diameter template was able to capture simulated tu-

mors up to 34 mm in diameter without accruing any additional false positives, using a threshold of 0.52.

In comparison to previously published CAD methods, the method presented herein is the only one except for Lee *et al.*[17] to employ a fully 3D approach. It is the first to utilize a frequency-domain-based 3D normalized cross-correlation coefficient computation and the first to employ image partial volume effects in 3D, which assist in making template matching efficient and sensitive to even very small nodules imaged with conventional pixel sizes. The paper is also the first to use 3D morphological operations for lung segmentation. Whereas other methods often perform a sequential series of computations including median filtering and selection for nodule candidate size, shape, contrast, and 3D connectivity, the 3D template matching approach incorporates all these processes into the calculation of a single parameter—the normalized cross-correlation coefficient. This obviates the need to perform an often complex search over a multidimensional parameter space for a global optimum. It is noted that the current realization of this algorithm running in MATLAB 6.5 on a 1.8 GHz Windows NT machine could be further optimized for computational speed using appropriate hardware and software modifications, thereby reducing considerably the 5 min per patient processing time. However, in its current state the method appears to take approximately the same or less computation time as previously published methods, at least for those methods for which computational estimates were given.

In 2001 Lee *et al.*[17] presented a template-matching technique that included 3D components, as mentioned in the Introduction. The advantages of the authors' current method, in comparison to Lee's approach, are that it uses asymmetric templates to address the non-isotropic resolution in CT scans, uses padding and variant overall template sizes to reduce the influence of background, assumes a more tumor-like uniform spherical profile model instead of a standard Gaussian profile, and searches the entire lung field using a fast Fourier domain algorithm rather than sparse sampling using a genetic algorithm. These differences eliminated the need for an extra computational step to reduce the number of false positives.

Future testing of the current methodology is planned with comparison to other previously defined detection methods. A larger-scale analysis is currently being conducted using the Early Lung Cancer Action Project (ELCAP)[8,10,11] lung image database, consisting of 50 sets of serial low-dose CT image datasets from lung patients. The major challenges of ELCAP data include lower signal-to-noise ratio (SNR) due to low exposure dose, moderate to severe streak artifacts; larger amount of data, an average of 255 slices per subject; and smaller nodules to detect, most are less than 7 mm in diameter and some are as small as 3 mm.

An active area of research is to quantify nodule volume and growth in order to differentiate active tumors from benign nodules. The ELCAP study found that 233 (23%) of the 1000 initial subjects presented with one to six pulmonary nodules on their first screening. Follow-up screenings on these 233 subjects determined that only 7 (3%) of these subjects had lung cancer. It is estimated that nodules that do not grow measurably in volume in a 6-month time-frame carry a malignancy risk of less than 10%.[45] Figure 4 demonstrates the influence of appearance model size on the correlation coefficient for each of a range of tumor sizes. These curves show that an optimal correlation value is obtained when the size of the appearance model matches the size of the given tumor. This observation suggests that accurate tumor size estimates may be obtained by adjusting the computer-generated appearance model size to obtain a maximal correlation value to a given tumor, having identified each tumor's location in a previous step. This will be tested in a future study.

ACKNOWLEDGMENTS

The authors wish to acknowledge helpful advice and input from David Fuller and Dr. Deborah Klein, and funding support from the American Cancer Society (RSG-02-155-01-CCE), the University of Rochester's RUBI program (Research for Undergraduates in Biomechanics and Imaging) (NSF-REU #EEC-0097470), and BrainLAB, AG.

[a]Author to whom correspondence should be addressed. Electronic mail: walter_odell@urmc.rochester.edu

[1]ACS, Cancer Facts and Figures 2006 (2006).
[2]Y. T. Lee, "Breast carcinoma: pattern of metastasis at autopsy," J. Surg. Oncol. **23**, 175–180 (1983).
[3]R. A. Willis, *The Spread of Tumours in the Human Body*, 3rd ed. (Butterworth, London, 1973).
[4]H. L. Kindler and K. L. Shulman, "Metastatic colorectal cancer," Curr. Treat. Options Oncolo. **2**, 459–471 (2001).
[5]P. Okunieff, R. E. Meyn, B. A. Teicher, C. R. Thomas, Jr., L. E. Gaspar, D. Raben, S. Giri, R. S. Lavey, A. T. Turrisi, III, G. P. Swanson, and S. R. Smalley, "Report from the Radiation Oncology Committee of the Southwest Oncology Group (SWOG): Research Objectives Workshop 2003," Am. J. Clin. Oncol. **26**, 522–529 (2003).
[6]M. C. Sampson, C. Huggins, M. Schell, P. Okunieff, A. Muhs, and A. Katz, "Hypofractionated stereotactic body radiation therapy for liver metastases," in the 47th Annual ASTRO Meeting, Denver, CO (2005).
[7]P. Okunieff, A. L. Petersen, A. Philip, M. T. Milano, A. W. Katz, L. Boros, and M. C. Schell, "Stereotactic body radiation therapy (SBRT) for lung metastases," Acta Oncol. **45**, 808–817 (2006).
[8]C. I. Henschke, D. I. McCauley, D. F. Yankelevitz, D. P. Naidich, G. McGuinness, O. S. Miettinen, D. M. Libby, M. W. Pasmantier, J. Koizumi, N. K. Altorki, and J. P. Smith, "Early Lung Cancer Action Project: overall design and findings from baseline screening [see comment]," Lancet **354**, 99–105 (1999).
[9]B. J. Hillman, "Economic, legal, and ethical rationales for the ACRIN national lung screening trial of CT screening for lung cancer," Acad. Radiol. **10**, 349–350 (2003).
[10]S. Sone, S. Takashima, F. Li, Z. Yang, T. Honda, Y. Maruyama, M. Hasegawa, T. Yamanda, K. Kubo, K. Hanamura, and K. Asakura, "Mass screening for lung cancer with mobile spiral computed tomography scanner [see comment]," Lancet **351**, 1242–1245 (1998).
[11]G. M. Strauss, R. E. Gleason, and D. J. Sugarbaker, "Screening for lung cancer. Another look; a different view [see comment]," Chest **111**, 754–768 (1997).
[12]M. Kaneko, K. Eguchi, H. Ohmatsu, R. Kakinuma, T. Naruke, K. Suemasu, and N. Moriyama, "Peripheral lung cancer: screening and detection with low-dose spiral CT versus radiography," Radiology **201**, 798–802 (1996).
[13]S. J. Swensen, J. R. Jett, J. A. Sloan, D. E. Midthun, T. E. Hartman, A. M. Sykes, G. L. Aughenbaugh, F. E. Zink, S. L. Hillman, G. R. Noetzel, R. S. Marks, A. C. Clayton, and P. C. Pairolero, "Screening for lung cancer with low-dose spiral computed tomography [see comment]," Am. J. Respir. Crit. Care Med. **165**, 508–513 (2002).
[14]S. D. Davis, "Through the 'retrospectoscope': a glimpse of missed lung

cancer at CT [comment]," Radiology **199**, 23–24 (1996).
[15]R. Kakinuma, H. Ohmatsu, M. Kaneko, K. Eguchi, T. Naruke, K. Nagai, Y. Nishiwaki, A. Suzuki, and N. Moriyama, "Detection failures in spiral CT screening for lung cancer: analysis of CT findings," Radiology **212**, 61–66 (1999).
[16]F. Li, S. Sone, H. Abe, H. MacMahon, S. G. Armato, III, and K. Doi, "Lung cancers missed at low-dose helical CT screening in a general population: comparison of clinical, histopathologic, and imaging findings," Radiology **225**, 673–683 (2002).
[17]Y. Lee, T. Hara, H. Fujita, S. Itoh, and T. Ishigaki, "Automated detection of pulmonary nodules in helical CT images based on an improved template-matching technique," IEEE Trans. Med. Imaging **20**, 595–604 (2001).
[18]B. Zhao, G. Gamsu, M. S. Ginsberg, L. Jiang, and L. H. Schwartz, "Automatic detection of small lung nodules on CT utilizing a local density maximum algorithm," J. Appl. Clin. Med. Phys. **4**, 248–260 (2003).
[19]H. Arimura, S. Katsuragawa, K. Suzuki, F. Li, J. Shiraishi, S. Sone, and K. Doi, "Computerized scheme for automated detection of lung nodules in low-dose computed tomography images for lung cancer screening," Acad. Radiol. **11**, 617–629 (2004).
[20]C. C. McCulloch, R. A. Kaucic, P. R. Mendonca, D. J. Walter, and R. S. Avila, "Model-based detection of lung nodules in computed tomography exams. Thoracic computer-aided diagnosis," Acad. Radiol. **11**, 258–266 (2004).
[21]J. W. Lee, J. M. Goo, H. J. Lee, J. H. Kim, S. Kim, and Y. T. Kim, "The potential contribution of a computer-aided detection system for lung nodule detection in multidetector row computed tomography," Invest. Radiol. **39**, 649–655 (2004).
[22]D. T. Lin, C. R. Yan, and W. T. Chen, "Autonomous detection of pulmonary nodules on CT images with a neural network-based fuzzy system," Comput. Med. Imaging Graph. **29**, 447–458 (2005).
[23]S. G. Armato, III, A. S. Roy, H. Macmahon, F. Li, K. Doi, S. Sone, and M. B. Altman, "Evaluation of automated lung nodule detection on low-dose computed tomography scans from a lung cancer screening program(1)," Acad. Radiol. **12**, 337–346 (2005).
[24]Z. Ge, B. Sahiner, H. P. Chan, L. M. Hadjiiski, P. N. Cascade, N. Bogot, E. A. Kazerooni, J. Wei, and C. Zhou, "Computer-aided detection of lung nodules: false positive reduction using a 3D gradient field method and 3D ellipsoid fitting," Med. Phys. **32**, 2443–2454 (2005).
[25]J. M. Goo, J. W. Lee, H. J. Lee, S. Kim, J. H. Kim, and J. G. Im, "Automated lung nodule detection at low-dose CT: preliminary experience," Kor. J. Radiol. **4**, 211–216 (2003).
[26]M. Fiebich, C. Wietholt, B. C. Renger, S. G. Armato, III, K. Hoffmann, D. Wormanns, and S. Diederich, "Automatic detection of pulmonary nodules in low-dose screening thoracic CT examinations," Proc. SPIE **3661**, 1434–1439 (1999).
[27]M. Fan, C. L. Novak, J. Qian, G. Kohl, and D. P. Naidich, "Automatic detection of lung nodules from multi-slice low-dose CT images," Proc. SPIE **4322**, 1828–1835 (2001).
[28]M. S. Brown, J. G. Goldin, R. D. Suh, M. F. McNitt-Gray, J. W. Sayre, and D. R. Aberle, "Lung micronodules: automated method for detection at thin-section CT—initial experience," Radiology **226**, 256–262 (2003).
[29]K. Kanazawa, Y. Kawata, N. Niki, H. Satoh, H. Ohmatsu, R. Kakinuma, M. Kaneko, N. Moriyama, and K. Eguchi, "Computer-aided diagnosis for pulmonary nodules based on helical CT images," Comput. Med. Imaging Graph. **22**, 157–167 (1998).
[30]M. L. Giger, K. T. Bae, and H. MacMahon, "Computerized detection of pulmonary nodules in computed tomography images," Invest. Radiol. **29**, 459–465 (1994).
[31]S. G. Armato, III, M. L. Giger, and H. MacMahon, "Automated detection of lung nodules in CT scans: preliminary results," Med. Phys. **28**, 1552–1561 (2001).
[32]J. P. Ko and M. Betke, "Chest CT: automated nodule detection and assessment of change over time—preliminary experience," Radiology **218**, 267–273 (2001).
[33]M. N. Gurcan, B. Sahiner, N. Petrick, H. P. Chan, E. A. Kazerooni, P. N. Cascade, and L. Hadjiiski, "Lung nodule detection on thoracic computed tomography images: preliminary evaluation of a computer-aided diagnosis system," Med. Phys. **29**, 2552–2558 (2002).
[34]M. Fiebich, D. Wormanns, and W. Heindel, "Improvement of method for computer-assisted detection of pulmonary nodules in CT of the chest," Proc. SPIE **4322**, 702–709 (2001).
[35]C. I. Henschke, D. F. Yankelevitz, I. Mateescu, D. W. Brettle, T. G. Rainey, and F. S. Weingard, "Neural networks for the analysis of small pulmonary nodules," Clin. Imaging **21**, 390–399 (1997).
[36]M. F. McNitt-Gray, E. M. Hart, N. Wyckoff, J. W. Sayre, J. G. Goldin, and D. R. Aberle, "A pattern classification approach to characterizing solitary pulmonary nodules imaged on high resolution CT: preliminary results," Med. Phys. **26**, 880–888 (1999).
[37]T. Hara, H. Fujita, Y. Lee, H. Yoshimura, and S. Kido, "Automated lesion detection methods for 2D and 3D chest X-ray images," in the International Conference on Image Analysis and Processing, Venice, Italy, 1999.
[38]T. Okumura, T. Miwa, J. Kako, T. Okumura, T. Miwa, J-i. Kako, S. Yamamoto, M. Matsumoto, Y. Tateno, T. Iinuma, and T. Matsumoto, "Image processing for computer-aided diagnosis of lung cancer screening system by CT (LSCT)," Proc. SPIE **3338**, 1314–1322 (1998).
[39]S. Lou, C. Chang, K. Lin, and T. Chen, "Object-based deformation technique for 3-D CT lung nodule detection," Proc. SPIE **3661**, 1544–1552 (1999).
[40]H. Taguchi, Y. Kawata, N. Niki, H. Satoh, H. Ohmatsu, R. Kakinuma, K. Eguchi, M. Kaneko, and N. Moriyama, "Lung cancer detection based on helical CT images using curved surface morphology analysis," Proc. SPIE **3661**, 1307–1314 (1999).
[41]M. S. Brown, M. F. McNitt-Gray, J. G. Goldin, R. D. Suh, J. W. Sayre, and D. R. Aberle, "Patient-specific models for lung nodule detection and surveillance in CT images," IEEE Trans. Med. Imaging **20**, 1242–1250 (2001).
[42]J. P. Lewis, *Fast Normalized Cross-Correlation* (Industrial Light & Magic, 1996).
[43]MathWorks, MATLAB (The MathWorks Inc.).
[44]R. Ambrosini, P. Wang, J. Victor, N. Sobe, and W. G. O'Dell, "Automatic detection and sizing of metastatic brain tumors using 3D template matching," in the 47th Annual AAPM Meeting, Seattle, WA, 2005.
[45]D. M. Libby, J. P. Smith, N. K. Altorki, M. W. Pasmantier, D. Yankelevitz, and C. I. Henschke, "Managing the small pulmonary nodule discovered by CT," Chest **125**, 1522–1529 (2004).